Direct-Drive–Ignition Designs with Mid-Z Ablators

Introduction

In laser-driven inertial confinement fusion (ICF),[1,2] a spherical capsule filled with deuterium–tritium (DT) is irradiated by direct laser illumination. Ablation of material from the target's outer surface generates a low-density coronal plasma and drives the implosion of the fuel shell through the rocket effect. To achieve ignition, the shell must be imploded at velocities >350 km/s to create a central hot spot enclosed within a cold and dense shell at stagnation. At the National Ignition Facility (NIF),[3] this implies that the hot spot of a capsule reaches both high areal density ($\rho R \sim 0.4$ g/cm^2) and high temperature ($T \sim$ 10 keV) while the total target areal density exceeds 1.5 g/cm^2. The DT fuel entropy is characterized by the adiabat α defined as the ratio of the shell pressure to the Fermi pressure of a fully degenerate gas. To achieve such conditions, low-adiabat implosions ($\alpha \le 3$) are required. The fuel adiabat is set during the first stage of the implosion, and it can be controlled by a precise tuning of the laser-induced, shock-wave timing. Low-adiabat implosions lead to higher areal densities and require less kinetic energy to achieve ignition conditions.

Shell preheat represents a major degradation mechanism for the fuel adiabat. Preheat is caused by the generation of hot electrons at densities below the critical density and results in degradation of the final compression. In the context of direct-drive implosions, the acceleration of electrons to high energies in the coronal plasma induced by the two-plasmon–decay (TPD)[4] instability can significantly reduce the target performance. Recent experiments on the OMEGA Laser System[5] have shown evidence of TPD-driven high-energy electrons during direct-drive implosions using D_2, DT, and plastic ablators.[6–8] Another critical area of concern to ICF is the unstable growth of target nonuniformitites resulting from hydrodynamic instabilities. During the implosion, the ablation surface between the expanding low-density coronal plasma and the high-density shell is subject to the Rayleigh–Taylor (RT) instability.[9,10] Therefore, perturbations imprinted on the target by nonuniform laser irradiation as well as modulations resulting from target fabrication will grow exponentially during the acceleration phase at a rate given by the modified Takabe formula[11,12] $\gamma(k) = \alpha\sqrt{kg/(1+kL)} - \beta k V_\mathrm{a}$, where α and β are coefficients depending on the ablation surface, k is the wave number of the perturbation, g is the acceleration, L is the density scale length at the ablation surface, and V_a is the ablation velocity. During the acceleration phase, the perturbation of the ablation surface feeds through to the inner shell surface, which becomes unstable when the shell is slowed down by the hot-spot gas. Excessive perturbation growth will reduce the total areal density level by raising the fuel adiabat and degrading the hot-spot conditions required for ignition. The unstable growth of these perturbations must be mitigated during the implosion to maintain the integrity of the shell at stagnation.

For ignition designs on the NIF, it is desirable to explore new ablators that mitigate both TPD and RT instabilities. Using materials of medium atomic number Z as ablators presents some advantages and has recently gained interest for direct-drive implosions. In laser-driven ablation of low-Z material, the optical laser radiation is absorbed around the critical density; the thermal energy is then transported by electrons from the absorption zone to the ablation surface. In the case of moderate-Z materials, the thermal radiation is directly absorbed into the ablator material, resulting in a double-ablation-front (DAF) structure[13,14] (electron-conduction and radiation-driven ablation fronts). Such a structure leads to a higher ablation velocity V_a and a longer density scale length L, thereby enhancing the ablative stabilization of RT growth at the electron front. Moreover, irradiation of mid-Z materials results in a better absorption of laser energy by inverse bremsstrahlung than low-Z ablators, leading to a higher electron temperature in the coronal plasma. The TPD instability gain is proportional to the inverse of the electron temperature[15] and will be increased for mid-Z ablators compared to plastic for equal density scale length. Many experiments have been recently performed to investigate these effects. A significant reduction in the hard x-ray signal for mid-Z ablators has been observed on OMEGA, suggesting the mitigation of the TPD-driven hot-electron generation.[16–19] Mid-Z targets have also demonstrated a reduced laser-imprint efficiency as well as a lower overall RT growth rate[20–22] on OMEGA and OMEGA EP.[23] Using higher-Z material ablators is expected, however, to present some downsides. The electron-heat conduction is lower for higher-Z materials, reducing the transport of the energy absorbed at subcritical densities to the ablation surface. The mass ablation rate and the resulting ablation pressure are consequently decreased, leading to a reduced hydrodynamic efficiency. Additionally, high-Z materials present higher radiation losses in the hot coronal plasma as well as more radiation preheat of the fuel. Furthermore, at the radiation front, the ablation velocity and density-gradient scale length are reduced and the RT growth is enhanced. Simulations of the overall stability are, therefore, needed to correctly assess the conflicting behavior of the two ablation fronts.

The aim of this article is to evaluate the viability of these ablator materials as a path for ignition target designs on the NIF. The following sections (1) introduce the one-dimensional (1-D) design and performance of three targets using different mid-Z ablators; (2) assess the linear stability of the TPD for these ablators; (3) explore the robustness to two-dimensional (2-D) single-mode and multimode perturbations under uniform drive; (4) display a polar-direct-drive beam configuration for each target; and, finally, (5) summarize the conclusions.

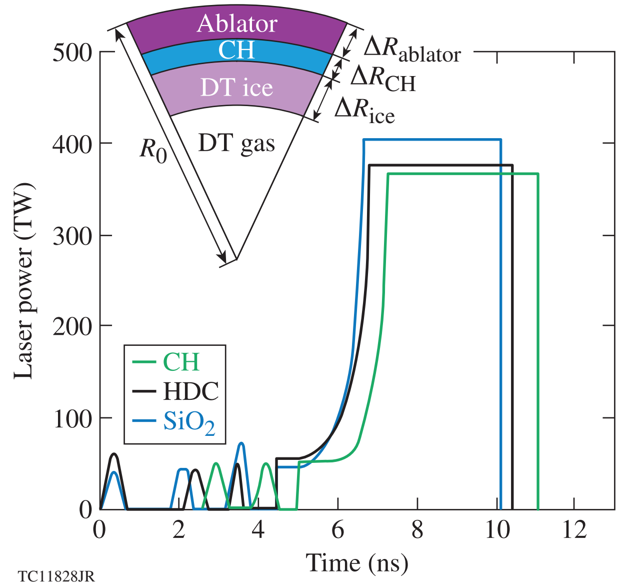

Figure 140.10
Schematic of the ignition target design and corresponding laser pulses for plastic (CH) (green curve), high-density carbon (HDC) (black curve), and glass (SiO_2) ablators (blue curve).

One-Dimensional Target Design Using Mid-Z Ablators

To investigate the viability of mid-Z ablator materials for ignition targets, three hydro-equivalent targets (same implosion velocity and fuel adiabat) with average atomic number ranging from 3.5 to 10 were designed. The ignition designs use pure plastic (CH, $\langle Z \rangle = 3.5$), high-density carbon (HDC, $\langle Z \rangle = 6$), and glass (SiO_2, $\langle Z \rangle = 10$) ablators. The plastic target is a variant of the 1-D–equivalent NIF ignition target described by Collins *et al.*[24] Throughout this article, the conventional plastic ablator design is used as a reference target for comparison with the alternative carbon and glass ablators.

The 1-D radiation–hydrodynamic code *LILAC*[25] has been used to optimize the target design and carefully tune the laser pulse to obtain comparable implosion performance for all three targets. Figure 140.10 presents the target design as well as the laser pulse for each ablator material. The targets consist of a solid-DT fuel capsule filled with DT gas surrounded by a plastic layer coated with an ablator layer. The plastic and ablator layer thicknesses are precisely chosen to keep the fuel on a low adiabat during the implosion, avoiding radiation preheat of the DT fuel at the end of the laser pulse. Triple-picket laser pulses followed by a low-intensity foot and a Kidder-like[26] isentropic rise to the main drive are used to carefully tune the fuel adiabat at the beginning of the implosion as well as raise the ablation velocity at the outer surface to reduce the RT growth rate according to the modified Takabe formula in the **Introduction** (p. 220). Each picket along with the low-intensity foot has a 300-ps rise time. The laser beams use a super-Gaussian intensity profile focused at the initial target radius R_0 with an exponent $\sigma = 2.2$.

One-dimensional *LILAC* simulations of mid-Z (HDC and SiO_2) ablators were performed using multigroup diffusion radiation transport; an average-ion model[27,28] in collisional radiative equilibrium (CRE)[29] for opacity tables; nonlocal thermodynamic equilibrium (non-LTE) tables for ionization; and a *SESAME*[30] equation of state (EOS). The low-Z ablator (CH) was modeled using the Astrophysical Opacity Table (AOT)[31] and *SESAME* EOS. All simulations used electron thermal transport described in the classical Spitzer-Härm[32] approximation with a flux limiter $f = 0.06$. The structure of the DAF in higher-Z materials strongly depends on the transport of radiation energy through the outer part of the shell. Although the plastic and carbon materials were properly modeled using 16 radiation groups, the glass ablator required 48 radiation groups to accurately describe the radiation transport and the resulting density and temperature profiles. We have found, however, that the results are relatively insensitive to details of the opacity tables. For instance, we compared simulations of the glass target using average-ion CRE tables and CRE tables generated by *PROPACEOS*[33] and found that the target gain changed by only 4%.

The target designs, laser parameters, and 1-D target performance for each ablator are summarized in Table 140.I. In this study, we consider plastic, high-density carbon, and glass with initial densities of 1.04, 3.5, and 2.32 g/cm^3, respectively. A plastic layer is introduced underneath the ablator in the mid-Z designs as a protective layer for the DT fuel from possible radiation preheat produced by the mid-Z ablator, as well as to reduce the density jump between the DT fuel and the ablator. The total energy in the pulses is 1.65 MJ, resulting in an implosion velocity of about 360 km/s for all three targets. The in-flight average fuel adiabat $\langle\alpha\rangle_{\text{fuel}}$ is kept at around 2. The ignition margin is determined by the level of multidimensional perturbations that the hot spot can tolerate to achieve marginal ignition. This parameter can be connected to a volume ratio described in 1-D by the minimal ratio of the clean volume at sub-ignition temperatures to the 1-D hot-spot volume[34,35] and is referred to as the minimum yield-over-clean (mYOC). The three targets have been designed to exhibit the same 1-D margin characterized by a mYOC ~ 40%. By doing so, all designs present a similar margin for ignition so that one can compare their robustness to ignition when the implosion is perturbed. Since mid-Z ablators are significantly heavier than plastic and exhibit lower hydrodynamic efficiency, the high implosion velocities required for ignition can be achieved only by limiting the total mass, thereby making the shells thinner. All targets are irradiated with a laser intensity ~1.2×10^{15} W/cm^2 and produce high gains. The glass target produces less thermonuclear energy because of a thinner DT layer. The in-flight aspect ratio (IFAR$_{2/3}$), defined as the ratio of the shell radius R to the shell thickness ΔR (defined between the inner fuel interface and the radiation front) when the shell inner surface is two-thirds of the initial target radius, is 27 for CH and 24 for HDC. The glass design presents two different values for the IFAR$_{2/3}$, characterizing the aspect ratio of the target by including only the radiation front or both the radiation and electron fronts. As a result of a decompressed ablator caused by stronger radiation effects, the distance between the inner fuel surface and the electron ablation front is large, resulting in an IFAR$_{2/3}$ value of 14. If the shell thickness ΔR is defined as the full-width-at-half-maximum density and, therefore, does not account for the zone between the electron and the radiation ablation fronts, the value of IFAR$_{2/3}$ including only the radiation front reaches 35, which is higher than for the plastic and carbon ablators.

Table 140.I: Target design and performances for the different ablator materials.

	CH	HDC	SiO_2
R_0 (μm)	1599	1550	1428
ΔR_{ice} (μm)	204	184	161
ΔR_{CH} (μm)	–	12	7
ΔR_{a} (μm)	43	13	23
E_{L} (MJ)	1.65	1.65	1.65
V_{imp} (km/s)	361	363	361
$\langle\alpha\rangle_{\text{fuel}}$	2.2	2.1	2.0
mYOC (%)	41	40	41
Gain	74.6	72.0	53.0
I_{L} ($\times 10^{15}$ W/cm^2)	1.2	1.3	1.5
IFAR$_{2/3}$	27	24	35/14

At such laser intensities, the radiation effects induce strong modifications of the hydrodynamic profiles. Figure 140.11 shows profiles of the radial mass density (solid lines) and electron temperature (dashed lines) at the end of the laser pulse for the three targets. The laser energy is absorbed by inverse bremsstrahlung, with the cross-section scaled as $\langle Z^2\rangle / \langle Z\rangle$, and, therefore, enhances the absorption in mid-Z materials. As a consequence, the temperature in the coronal plasma is higher for the carbon and glass ablators (5.3 and 6.2 keV, respectively) than for the plastic ablator (~4.9 keV). In the case of plastic targets, the absorbed laser energy is transferred to thermal electrons that drive the electron ablation front. For mid-Z targets,

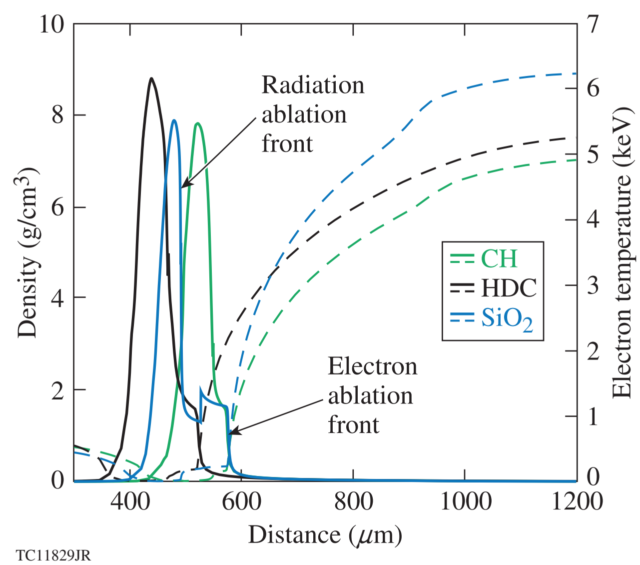

Figure 140.11
Profiles of radial mass density (solid curves) and electron temperature (dashed curves) at the end of the laser pulse for the plastic (11 ns) (green curve), carbon (10.4 ns) (black curve), and glass (10.1 ns) (blue curve) targets.

the high-temperature corona plasma emits strong radiation that deposits its energy in more-opaque regions of the target, where the temperature is lower and the density is higher, thereby driving the radiation ablation front. This DAF structure is clearly visible in Fig. 140.11.

Despite a better overall absorption, the hydroefficiency of ICF designs using mid-Z ablators is expected to be altered in comparison with low-Z material targets. The mass ablation rate and ablation pressure are decreased as the thermal conduction scales as $1/Z_{\text{eff}}$, where $Z_{\text{eff}} = \left\langle Z^2 \right\rangle \Big/ \left\langle Z \right\rangle$. As a result of less-effective heat transport and radiation losses in high-Z coronal plasmas, the hydrodynamic efficiency is reduced. It has also been observed that the conduction zone is much shorter for mid-Z materials than for plastic, which can have a compensating effect (that level depending on the material and its density) for the conduction losses.[17]

The three targets have been designed in 1-D to achieve similar implosion characteristics, high-gain performances, and ignition margins. The remaining sections compare mid-Z to plastic ablators with respect to hot-electron generation and hydrodynamic instability growth.

Mitigation of the Two-Plasmon–Decay Instability

The performance of low-adiabat direct-drive implosions can be severely degraded by hot-electron preheating at laser intensities for which the quarter-critical electron density is above $\sim 5 \times 10^{14}$ W/cm^2. Recent experiments on OMEGA have shown that the hard x-ray signals generated by hot electrons from the TPD instability rise sharply at laser intensities above 5×10^{14} W/cm^2 and then saturate for plastic ablator targets.[7,8,36] The measured hot-electron temperature is in the 50- to 100-keV range when the laser intensity increases from 5×10^{14} to 10^{15} W/cm^2 and the fraction of total laser energy deposited into hot electrons saturates at a level of a few percent[18,37–39] at 10^{15} W/cm^2 in planar targets, which is sufficient to significantly raise the fuel adiabat. Implosions at adiabats relevant to the high-gain designs for the NIF require strategies to mitigate hot-electron preheat.

A straightforward path to preheat mitigation is to use different ablator materials to modify the hydrodynamic profiles and increase the instability threshold for the TPD instability. OMEGA experiments in the intensity range of 3 to 7×10^{14} W/cm^2 have demonstrated lower hot-electron production for silicon, germanium, and chlorine-doped plastic ablators.[17–19] The reduction reaches a factor of 10 for an aluminum ablator,[17] which may be a result of a near-threshold effect. The hard x-ray signals caused by TPD-driven hot electrons were reduced by a factor of 40 in implosions using glass ablators compared to plastic[16] at an intensity of 10^{15} W/cm^2. The measured hot-electron temperature was reduced by a factor of 2 with the glass ablators, resulting in a reduction of the shell preheat by more than an order of magnitude.

The threshold[15] for triggering the absolute TPD instability of a plane electromagnetic (EM) wave in an inhomogenous plasma is given approximately by the parameter $\eta = L_{\text{n}} \times I_{14} \Big/ \left(230\, T_{\text{e}}\right) = 1$, where L_{n} is the density scale length in μm, I_{14} is the EM wave intensity in units of 10^{14} W/cm^2, and T_{e} is the electron temperature in keV, with all these parameters being evaluated at quarter-critical density. According to this formula, ablators of moderate-Z numbers exhibit several advantages over low-Z materials: a higher electron temperature T_{e}; a better absorption in the corona, leading to a lower-intensity I_{14} at quarter-critical density; and a shorter density scale length L_{n} because of the slow expansion of the heavier fluid. However, the TPD instability presents a nonlinear behavior, leading to the saturation of the growth rate at high intensities.

The collisional damping of Langmuir waves (LW's) plays an important role in materials with a higher Z_{eff} than plastic. The linear growth rate of the TPD instability obtained by Simon *et al.*[15] has been generalized to account for the LW collisional damping and can be expressed as

$$\hat{\gamma} = \frac{L_{\text{n}} I_{14}}{230\, T_{\text{e}}} - 1 - \frac{0.3\, Z_{\text{eff}} L_{\text{n}} \sqrt{I_{14}}}{230\, T_{\text{e}}^{5/2}}. \tag{1}$$

The Z_{eff} number of the three targets introduced in the previous section varies between 5.3 for CH, 6 for HDC, and 10.8 for SiO_2. Figure 140.12(a) shows the temporal evolution of the electron temperature at quarter-critical density, and Fig. 140.12(b) shows the generalized TPD growth rate introduced in Eq. (1) for the three designs. The temporal axis has been normalized to the beginning of the main drive for each target. The electron temperature has been increased by ~1500 eV and ~500 eV, respectively, for the glass and carbon targets compared to the plastic target (~4.0 keV). Because of a higher temperature and a shorter density scale length (~450 μm for SiO_2 and ~550 μm for CH), the first term of the right-hand side of Eq. (1) is decreased for mid-Z materials. However, the effect of collisional damping on the TPD growth rate [represented by the last term of the right-hand side of Eq. (1)] is strongly dependent on the temperature and is also correlated to the effective atomic number. As a result, the carbon target and especially the glass target benefit from a higher collisional damping of LW than the

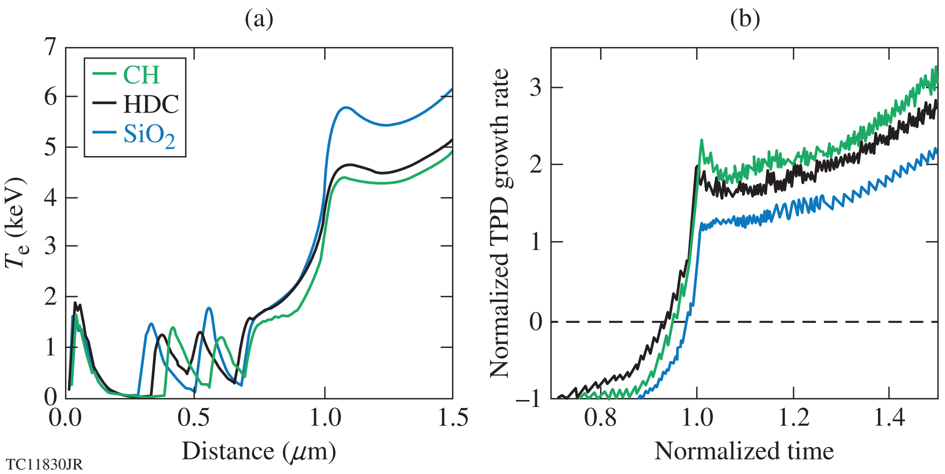

Figure 140.12
Temporal evolution of (a) the electron temperature at quarter-critical density and (b) the normalized two-plasmon–decay (TPD) growth rate for the plastic (green curve), high-density carbon (black curve), and glass ablators (blue curve).

plastic target. The absolute TPD instability is triggered when the generalized growth rate is positive $\hat{\gamma} > 0$. One can observe in Fig. 140.12(b) that the three targets will be affected by this instability. The growth rate is still lower, however, for mid-*Z* than low-*Z* ablators, presumably resulting in a saturation at a lower level of conversion fraction of energy into hot electrons.

Nonlinear effects such as the collisional damping of Langmuir waves (LW's) and the collisional damping of ion-acoustic waves (IAW's) can be accounted for by performing simulations[40] based on the Zakharov model of TPD.[41,42] These calculations describe the growth and the nonlinear saturation of the TPD instability. It has been shown that materials with a higher effective atomic number $Z_{\text{eff}} = \langle Z^2 \rangle / \langle Z \rangle$ lead to TPD saturation at similar intensities (~10^{15} W/cm^2) but present a lower fraction of energy converted into hot electrons[43] (approximately half the level for glass material compared to plastic). On the basis of Ref. 43, mid-*Z* materials appear to benefit from higher collisional damping of LW as well as from weaker damping of IAW.

For OMEGA implosions at intensities above 10^{15} W/cm^2, the stimulated Raman scattering (SRS) instability can also couple laser energy into hot electrons.[44] The laser-intensity threshold for excitation of SRS[45] is $I_{16} \simeq 10\left(T_e / L_n^{4/3}\right)$, where I_{16} is in units of 10^{16} W/cm^2, L_n is in μm, and T_e is in keV at quarter-critical density for a laser wavelength of 0.351 μm. Another laser–plasma interaction (LPI) issue for coupling laser energy to the plasma is cross-beam energy transfer (CBET). The uniform illumination of targets with many overlapping laser beams creates favorable conditions to allow for the transfer of energy among beams, scattering the light outward and reducing laser coupling. Calculations have shown that CBET becomes an important factor in OMEGA implosions[46] at intensities above 5×10^{14} W/cm^2. The dependence of the gain rate of CBET on atomic number *Z* is complex but can be approximated[47] as 1/*Z*. Consequently, the higher temperature and shorter density scale length exhibited in mid-*Z* hydrodynamic profiles indicate a mitigation of SRS-driven hot electrons as well as a reduction of CBET.

Hydrodynamic Stability of Moderate-*Z* Ablator Targets Under Uniform Drive

In this section, we investigate the hydrodynamic stability properties of mid-*Z* ablators. Theoretical[14,48] and numerical studies[49] have shown that the DAF structure characteristic of mid-*Z* materials can aid in the overall stabilization of the target. Reduced RT growth rates have been observed experimentally in bromine,[13,50] silicon, and germanium-doped plastic[20,21] compared to pure plastic. Therefore, the viability of mid-*Z* ablators as a potential ICF direct-drive–ignition ablator is studied and compared to the hydrodynamic performance of plastic shells.

1. Single-Mode Simulations

The DAF structure of mid-*Z* ablators affects the hydrodynamic stability. One-dimensional simulations are used to characterize the DAF properties. In Fig. 140.13, the 1-D *LILAC* simulations show the density profiles taken 500 ps after the beginning of the linear phase of the RT instability. The DAF structures are clearly visible for the SiO_2 and HDC targets, and a less-pronounced DAF can also be observed for the CH target. In ignition-scale targets, there is sufficient radiation generation and absorption to produce a DAF structure, even in CH ablators. The high ablation velocity caused by the small peak density (around 1 g/cm^3) at the electron front results in a strong ablative stabilization at the electron front in the DAF structure. As a consequence, the electron front is expected to be stable and only the RT instability at the radiation front must be considered. Unless otherwise indicated, the studies in the

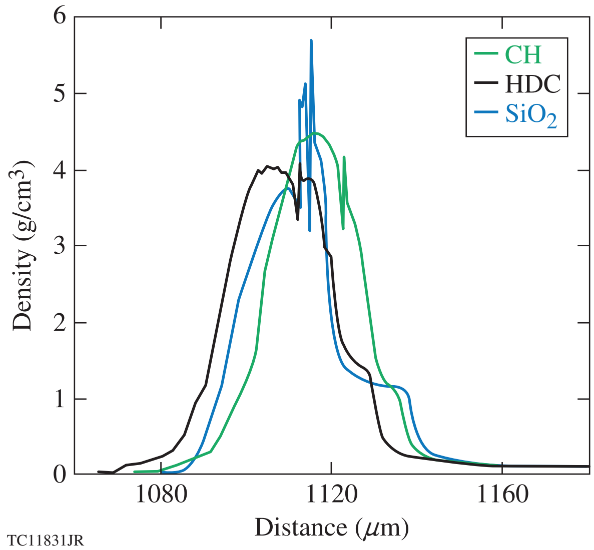

Figure 140.13
Radial mass-density profiles 500 ps after the beginning of the linear phase of the Rayleigh–Taylor (RT) instability for the plastic (8.6 ns) (green curve), carbon (8.0 ns) (black curve), and glass (7.5 ns) (blue curve) targets.

remainder of this article address the radiation front. The ablation velocity V_a, shell acceleration g, and density scale length L have been extracted from the 1-D simulations at the radiation front for each target, and these values have been averaged over the linear phase of the RT growth. As one can observe in Fig. 140.13, the density scale length at the radiation front reduces when the atomic number increases with values of 3.8, 3.0, and 1.5 μm for CH, HDC, and SiO_2 ablators, respectively. The shell acceleration is slightly greater for the mid-Z materials ($\sim 8.0 \times 10^{15}$ cm/s^2) than for plastic ($\sim 7.5 \times 10^{15}$ cm/s^2). The ablation velocity is also slightly increased for SiO_2 ($\sim 3.0 \times 10^5$ cm/s) compared to plastic ($\sim 2.8 \times 10^5$ cm/s), while the HDC target exhibits the higher value ($\sim 3.5 \times 10^5$ cm/s). According to the RT linear growth rate formula in the **Introduction** (p. 220), larger shell acceleration and smaller density scale length result in an increased growth of the classical RT instability at the radiation front for the mid-Z targets. The higher mass ablation rate for the SiO_2 and especially for the HDC targets has, however, a stabilizing effect on the radiation ablation front. The slightly higher classical RT growth in the HDC target is, therefore, sufficiently compensated by the increase in the ablation velocity, while the SiO_2 target remains slightly more unstable than the CH target.

The RT growth in the DAF structure was investigated using the 2-D arbitrary Lagrangian–Eulerian radiation–hydrodynamics code *DRACO*.[51] This code has been recently benchmarked for single-mode linear growth against flat-foil experiments with mid-Z ablators on OMEGA.[52] The *DRACO* simulations were performed using the same physical models used in the *LILAC* simulations presented in **One-Dimensional Target Design Using Mid-Z Ablators** (p. 221). The RT growth rate is calculated for several perturbation wave numbers during the linear phase of the instability by extracting the slope of a single perturbation-mode amplitude evolution in time at the radiation ablation front from the *LILAC* simulations. The RT growth is investigated for a single perturbation imposed on the target's outer surface of an initial amplitude chosen to keep the RT modes in the linear regime over the entire acceleration phase in the range of $20 < \ell < 200$. The 2-D simulations were performed using 20 azimuthal cells per half-wavelength of the perturbation and six radial cells in the interval outside the ablation surface defined by $1/k$ to ensure a good numerical resolution convergence and an accurate physical solution. The laser absorption was computed with sector ray tracing.

The amplitude of the perturbation grows exponentially as $\exp(\gamma t)$, where γ is the linear growth rate during the acceleration phase, until it reaches the nonlinear phase when its amplitude exceeds $\sim 0.1\ \lambda$. At this point, more rapidly growing high harmonics appear and the nonlinearity of the perturbation begins. The initial amplitude for increasing mode numbers was decreased in order to keep the harmonic growth lower than 10% of the fundamental wavelength. The linear growth factor $\exp(\gamma t)$ is computed over the entire acceleration phase up to the time where the velocity reaches its peak value. Figure 140.14 shows the linear growth factor as a function of the mode number of the perturbation imposed on each target. In this figure, the initial amplitude of the mode is chosen right at the beginning of the acceleration phase, which is well past the phase inversions produced by shock propagation through the multiple interfaces occurring during the Richtmyer–Meshkov (RM) phase in the early stages of the illumination. The growth factor strongly increases with the mode number but remains similar for the three targets for low-mode numbers up to $\ell = 70$, while the glass target exhibits a larger growth than the plastic and carbon targets above $\ell = 70$. Furthermore, the growth factor depends on the perturbation wave number k and is related to the mode number ℓ by $k = \ell/R$, where R is the target's outer radius. Keeping in mind that the initial radius of the glass target is smaller than for the carbon and plastic targets, the wave number will be higher for SiO_2 for a specific mode number ℓ, which will tend to increase the corresponding growth rate in comparison with HDC and CH. The most-damaging modes are those with wave numbers scaling as $k\Delta R \sim 1$, corresponding to $\ell \sim R\Delta R$. Longer wavelengths grow more slowly while shorter

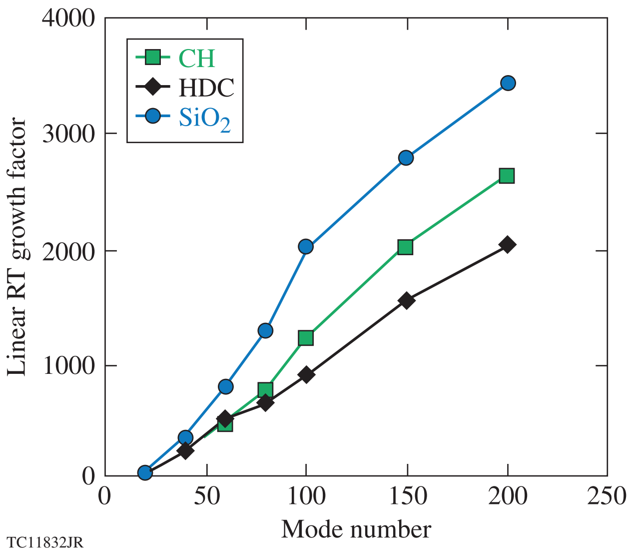

Figure 140.14
Linear growth factor of the Rayleigh–Taylor instability during the acceleration phase depending on the mode number of the perturbation for the plastic (green line with squares), high-density carbon (black line with diamonds), and glass ablators (blue line with circles).

wavelengths saturate at smaller amplitudes. Consequently, the integrity of the shell is mostly affected by ℓ modes in the range of $20 < \ell < 40$. Even when considering an uncertainty factor of 2, the linear growth factors in this range are similar for all three designs.

Carbon ablators exhibit lower growth than plastic for higher-mode numbers. The RT growth for the carbon target tends to saturate and enter the nonlinear phase earlier than the plastic target for higher-mode numbers. This could be an effect of the coupling between the perturbations growing at both the radiation and electron ablation fronts while no coupling occurs in the plastic target. According to Fig. 140.13, the standoff distance between the two fronts is small for the HDC target, which could lead to a more-effective coupling of the high-mode perturbations between the two fronts, while in comparison with the glass target where the large standoff distance reduces the coupling between the fronts.

Mid-*Z* ablators exhibit stability properties similar to those of plastic, especially for $\ell < 100$. A realistic implosion introduces, however, multiple sources of multimode perturbations that grow into the nonlinear regime (surface roughness, ice roughness, and laser imprint seeded by the multibeam laser irradiation). Therefore, multimode simulations must be performed to accurately assess the target performance.

2. Laser Drive and Capsule Nonuniformities

The stability of each target to multiple sources of nonuniformities is first investigated for uniform illumination. For these studies, the baseline configuration is the 1-D design, and the illumination pattern extracted from the 1-D simulation is used to irradiate the target. Several multimode simulations were performed in half-sphere geometry, using the code *DRACO*, to evaluate the overall hydrodynamic stability to capsule and single-beam nonuniformities. Capsule nonuniformities include inner-surface roughness of the DT ice layer and outer-surface roughness of the ablator. Laser nonuniformities are studied by including multimode laser imprint from single-beam irradiation. Each of these sources of perturbations is added individually to the baseline implosion for each target.

The effect of inner DT-ice roughness on the target performance is quantified by computing the gain normalized to the 1-D results while varying the amplitude of the perturbation. Perturbation modes up to $\ell = 50$ are included with the amplitude of the perturbation decaying as ℓ^{-1}. The simulations are carried out using at least 12 azimuthal cells for the shortest wavelength. The NIF specification for the roughness of the inner DT-ice surface is set at 1-μm rms (root mean square). Figure 140.15(a) shows the target performance as a function of the initial amplitude of the inner DT-ice layer's roughness for each target. All three designs exhibit high target-gain reduction for ice roughness above 6-μm rms corresponding to 6× the NIF specification. Similarly, the capsule's sensitivity to the roughness of the ablator's outer surface is evaluated by imposing a multimode spectrum of perturbations of various amplitudes. Since the initial amplitude of the ice-roughness spectrum is set to scale as ℓ^{-1} in this study, the growth of high modes has a rather negligible effect on the overall stability so the ice-roughness power spectrum is chosen to include modes up to $\ell = 50$. The NIF specification for this source of perturbation is set at about 115-nm rms. Figure 140.15(b) shows the normalized target gain as a function of the surface roughness of the ablator's outer surface. All three targets achieve close to 1-D gains for up to 1-μm rms, corresponding to more than 8× the NIF specification. In conclusion, all three targets are robust to both the inner-ice-surface and outer-surface roughnesses well above NIF specifications.

The largest multimode perturbations in direct-drive ICF implosions are seeded by nonuniformities in the laser-beam intensity that imprint on the target early in the laser pulse and grow during the acceleration phase. Multimode simulations of laser imprinting using realistic single-beam laser nonuniformities, including even modes up to $\ell = 100$ to account for

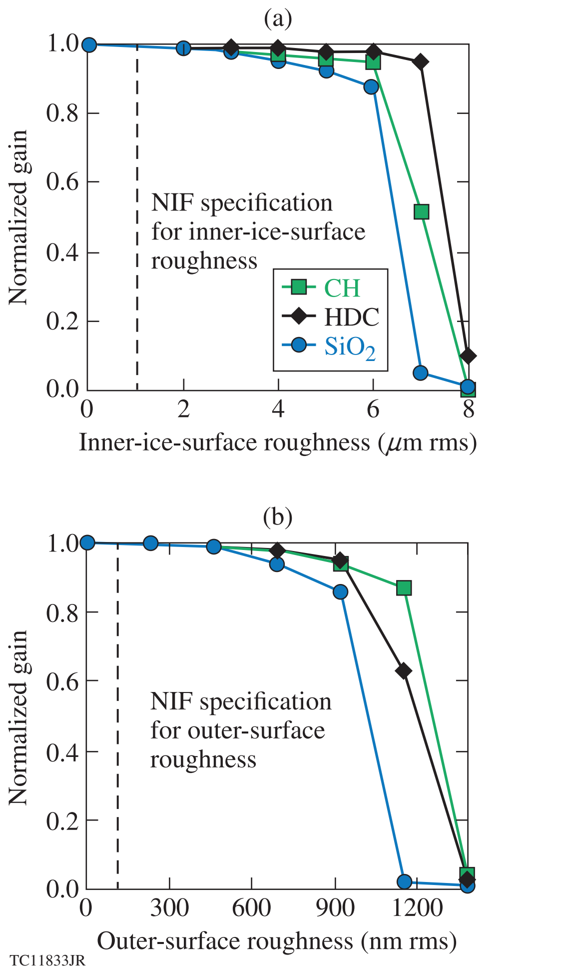

Figure 140.15
Normalized gain as a function of (a) ice roughness and (b) surface roughness for plastic (green curve), carbon (black curve), and glass (blue curve) targets in the uniform laser configuration.

the most-dangerous modes (see **Single-Mode Simulations**, p. 224), are performed for the three materials. These multi-mode illumination nonuniformities are modulated in time using 2-D smoothing by spectral dispersion (SSD)[53] as a method of temporal beam smoothing. Figure 140.16 shows the temporal evolution of the rms deviation of the density at the radiation ablation front extracted from half-sphere simulations of the three designs that included single-beam laser imprint. The RM-unstable phase can be observed for the three targets during the three-picket and the pre-foot laser pulses, while the RT-unstable phase starts at the beginning of the acceleration phase at 7.2 ns, 6.8 ns, and 6.6 ns for the CH, HDC, and SiO_2 targets, respectively. The RT growth rate at the radiation ablation front is slightly higher for the glass designs than for carbon and plastic designs, showing a comparable temporal growth of the rms deviation of density. This deviation saturates at the end of the acceleration phase and is not shown after the RT growth enters the nonlinear regime. The glass and plastic designs exhibit a smaller seed amplitude at the beginning of the RT-unstable phase (0.14 and 0.11 μm, respectively) about half the size of the carbon target (0.21-μm rms) because of phase inversions resulting from shock breakouts at the different interfaces during the RM-instability phase. Figure 140.17 shows

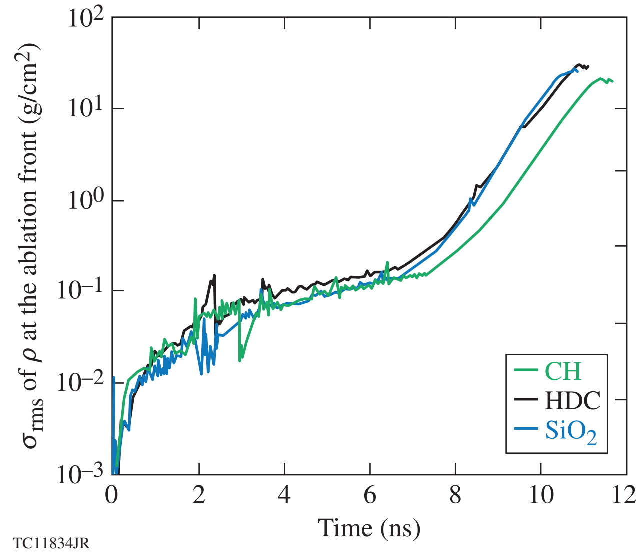

Figure 140.16
Temporal evolution of the σ_{rms} of density at the radiation ablation front for the CH (green line), HDC (black line), and SiO_2 (blue line) targets.

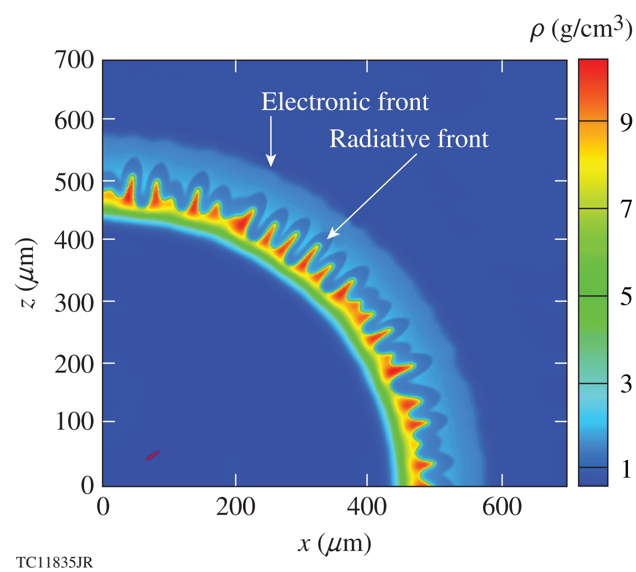

Figure 140.17
Simulated density contour plot of the uniform design subjected to laser imprint perturbations at the end of the pulse for the SiO_2 target.

the density contour plot of the simulation of laser imprint on the glass target at the end of the laser pulse. It clearly appears that the electron front remains stable during the acceleration phase while the RT instability has already strongly developed at the radiation front.

Perturbations at the unstable radiation ablation front are fed to the inner surface of the solid DT fuel during the acceleration phase. These perturbations seed the RT instability during the deceleration phase. The inner surface of the shell becomes unstable when the imploding material starts to decelerate because of the pressure exerted by the inner gas on the shell. When the amplitude of the final perturbation of the inner solid DT surface is comparable to the hot-spot radius, the ignition process can be severely compromised. Figure 140.18 displays the density contour plots for the (a) CH, (b) HDC, and (c) SiO_2 designs in the presence of laser imprinting with even modes up to $\ell = 100$ at time of ignition. The white solid lines indicate the ion temperature inside the hot spot in keV. The solid DT inner surface is more distorted for mid-Z ablators because of a thinner DT layer and more-effective feedthrough. The glass design exhibits a more-distorted shell than the other designs because of a higher in-flight aspect ratio. However, the overall stability of these targets to laser imprint perturbations exhibits enough margin to achieve ignition and produce high gains of 68 for CH, 62 for HDC, and 39 for SiO_2, corresponding to 91%, 86%, and 74%, respectively, of the nominal gain achieved for an unperturbed implosion.

Based on the above results, mid-Z ablator targets exhibit a performance similar to that of the conventional plastic ablator target under uniform laser irradiation. Mid-Z ablators do not mitigate the RT growth of perturbations seeded by either fabrication defects or laser-drive nonuniformities for ignition-scale target designs. The stabilizing effect observed at sub-ignition scale[13,20,21,50] does not significantly affect the growth at the radiation front because the radiation and electron ablation fronts are strongly decoupled during the acceleration phase. Nevertheless, mid-Z ablators for ignition targets mitigate the TPD instability while retaining stability properties similar to plastic ablators.

Two-Dimensional Polar-Direct-Drive Configuration for Moderate-Z Ignition Targets

Because of its current indirect-drive laser configuration, standard direct-drive experiments using uniform illumination are not feasible on the NIF. To achieve the most-uniform target illumination for direct drive, repointing some of the beams from the x-ray drive configuration toward the equator should maintain enough symmetry in the drive pressure to achieve the ignition conditions [polar direct drive (PDD)[54]]. The oblique incidence of the repointed beams on the target decreases the coupling of the laser energy to the target, affecting its hydrodynamic efficiency and symmetry. Recent numerical[24,55–60] and experimental[55,61–64] studies have investigated direct-drive plastic target performances in a PDD configuration on both OMEGA and the NIF.

The 192 NIF beams are grouped into 48 clusters of four beams, with each cluster forming a quad. In the x-ray drive configuration, 24 *quads* from each hemisphere are pointed at different angles with respect to the polar axis, forming four

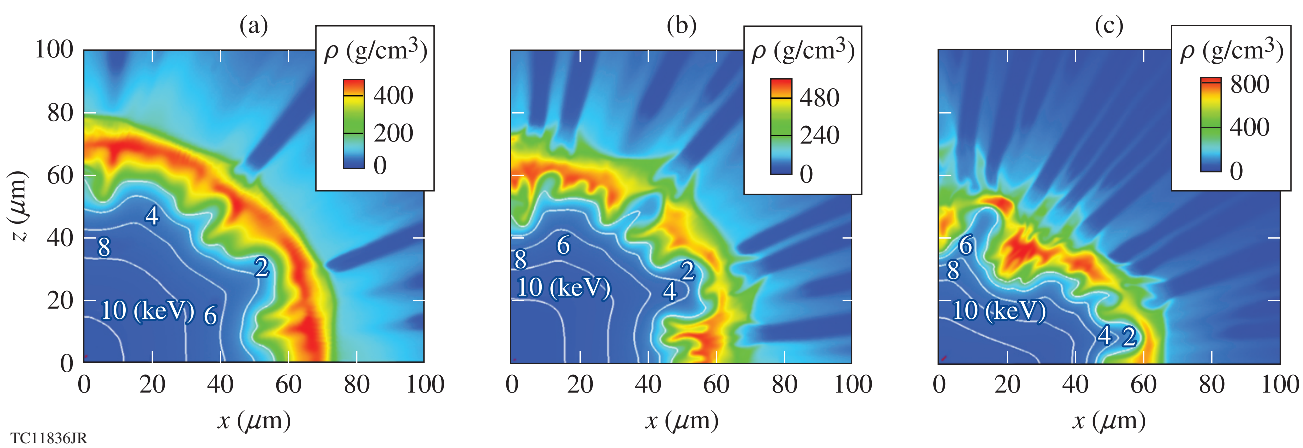

Figure 140.18
Simulated density contour plots of the 2-D uniform design subjected to laser-imprint perturbations at the onset of ignition for (a) the CH target at t = 11.9 ns, (b) the HDC target at t = 11.4 ns, and (c) the SiO_2 target at t = 11.1 ns. The white solid lines indicate (in keV) the ion temperature inside the hot spot.

rings of beams: four quads at 23.5°, four quads at 30°, eight quads at 44.5°, and eight quads at 50°. In the PDD configuration, the beams are repointed toward the equator: The four quads at 23.5° and 30° are repointed to 24.5° and 44°, respectively. The ring of beams at 44.5° is split into four quads repointed to 44° and four quads to 86°. The eight quads at an initial angle of 50° are all repointed to 86°. Therefore, the PDD configuration uses only three rings of beams at 24.5° (eight quads), 44° (16 quads), and 86° (24 quads) labeled, respectively, *polar*, *mid-latitude*, and *equatorial* beams to produce optimal results for drive uniformity.

Because the equatorial beams exhibit a greater obliquity to the target, they deposit their energy farther away from the ablation front than the polar beams, thereby lowering the laser absorption and reducing the drive efficiency. Therefore, the laser intensity must be increased near the equator relative to the pole to compensate for this effect. As the target implodes, time-dependent effects, as well as the multidimensional effects caused by lateral heat flow arising from temperature variations in the laser deposition region, must be considered. Furthermore, the absorption and hydrodynamic efficiency varies for different ablators. The irradiation strategy must also address the angular difference in hydrodynamic efficiency resulting from variations in density depending on the laser absorption around the target. The NIF can provide different laser pulses for each quad. To account for all these effects, different pulse shapes were used for the three rings of beams. In this study, each design required a dedicated beam-pointing strategy for the equatorial beams and time-dependent relative energy balance among the rings of beams, depending on the ablator. To illustrate this requirement, the laser pulses used to create the power balance between rings are presented in Fig. 140.19 for the SiO_2 design. Single-beam power for the polar (green curve), mid-latitude (blue curve), and equatorial (black curve) rings of beams is presented. To offset the reduction in laser drive, additional energy is required in the PDD configuration compared to the uniform illumination presented in **Hydrodynamic Stability of Moderate-Z Ablator Targets Under Uniform Drive** (p. 224). A total laser energy of 1.74 MJ, 1.75 MJ, and 1.76 MJ is used to achieve ignition of the CH, HDC, and SiO_2 designs, respectively.

Further optimization can be obtained by optimizing the laser-spot profiles compared to a uniform irradiation. It has been shown[24,59] that low super-Gaussian–order beam profiles are highly desirable for PDD laser-spot shapes since the energy on target can be efficiently redistributed by reducing the peaked illumination on the pole when using lower super-

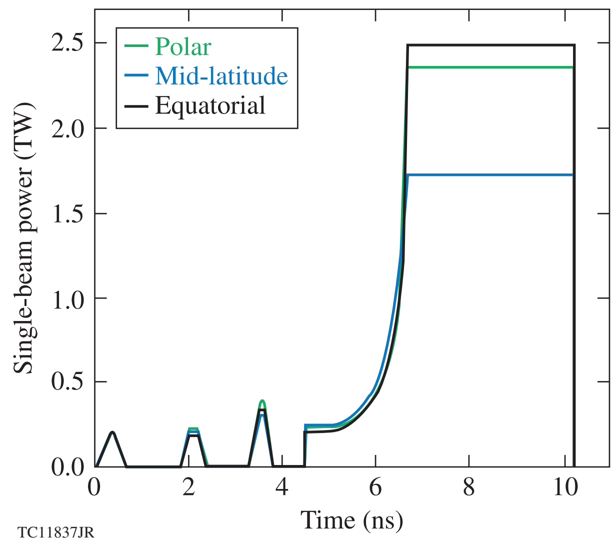

Figure 140.19
Single-beam power for the polar (green curve), mid-latitude (blue curve), and equatorial (black curve) rings of beams for the SiO_2 design.

Gaussian order. In this study, the on-target intensity is produced by a circular super-Gaussian profile using an order of 3.4 for the pole and 2.2 for the mid-latitude beams. To improve the absorption uniformity in the equatorial region, the laser-spot profile is obtained by adding an elliptical profile on the initial profile for the equatorial rings of beams. This ellipse is characterized by a super-Gaussian order of 2.2, a relative amplitude of 10% to 30% (depending on the ablator material) relative to the circular spot, an ellipticity of 3, and an offset of 15% of the initial target radius toward the equator relative to the center of the circular-spot profile. The focal-spot radius of the circular ellipse is set to the initial target radius for all rings of beams. Each irradiation region will require a different type of phase plate for each design presented in this article.

Polar-direct-drive simulations of the three designs were performed using the 2-D *DRACO* code including a three-dimensional (3-D) laser ray-trace modeling of the NIF beams and using a flux limiter of $f = 0.06$. The relative energy among the beams, the beam pointing, and the beam spot shapes were varied to find an optimal configuration of the target drive uniformity for each design. These calculations consider only the nonuniformities arising from beam pointing and energy balance in between rings of beams inherent to a PDD laser configuration. Simulated density contour plots along with ion temperatures (in keV) inside the hot spot (white solid lines) at the onset of ignition for the CH ($t = 12.03$ ns), HDC ($t = 11.33$ ns), and SiO_2 ($t = 11.15$ ns) targets are presented in Fig. 140.20.

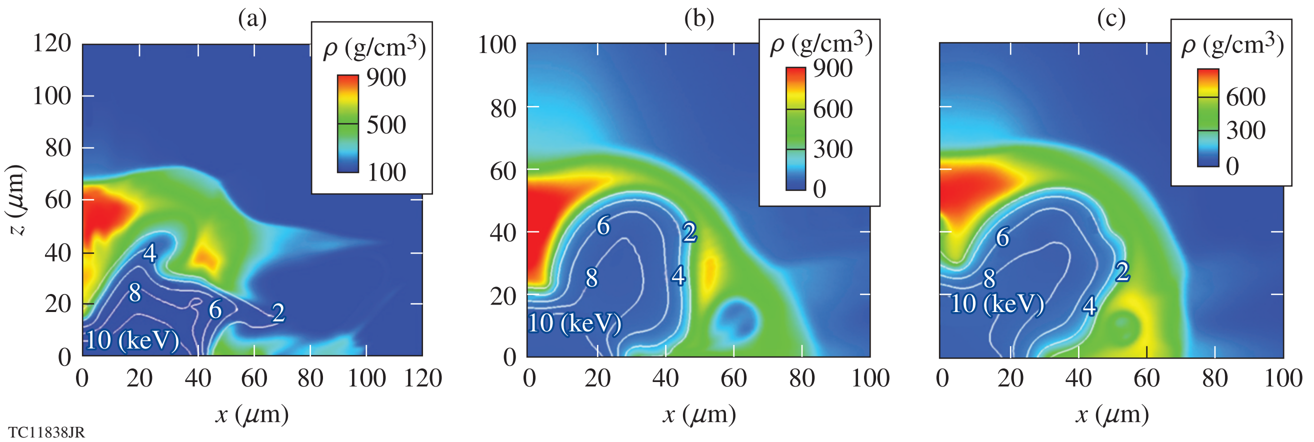

Figure 140.20
Simulated density contour plots at the onset of ignition of the (a) CH target at t = 12.03 ns, (b) HDC target at t = 11.33 ns, and (c) SiO_2 target at t = 11.15 ns in the polar-direct-drive configuration. The white solid lines indicate the ion temperature inside the hot spot in keV.

All designs present a shell shape dominating $\ell = 4$ mode of nonuniformity characteristic of PDD implosions and exhibit similar shell integrity. All designs achieve high target gain using the PDD irradiation configuration. Values of 68 for CH, 65 for HDC, and 44 for SiO_2 are achieved corresponding to 91%, 90%, and 83%, respectively, of the nominal gain achieved for an unperturbed implosion under uniform illumination. Investigation of each design's robustness in this configuration is underway. The effects of laser imprinting and capsule non-uniformities on the PDD designs will be examined in future work. In addition, the recent developments in the *DRACO* code will allow us to investigate the nonlocal effects of heat transport[65,66] as well as the effects of CBET in laser coupling and absorption symmetry.

Conclusions

The use of materials of medium atomic number Z as ablators is considered as a possible path for direct-drive implosions to mitigate the detrimental effects of the TPD instability. Three hydro-equivalent ignition targets using pure plastic (CH), HDC, and glass (SiO_2) ablators have been designed to accelerate the DT fuel to the same implosion velocity and adiabat.

It has been shown that because of a higher temperature and a shorter density scale length, the threshold for the TPD instability is increased for mid-Z materials. Moreover, the carbon target and especially the glass target benefit from a higher collisional damping effect on the TPD growth rate than for the plastic target. The growth rate is lower for mid-Z than low-Z ablators, resulting in reduced hot-electron energy and temperature. In addition, the higher plasma temperature and shorter density scale length in mid-Z coronal profiles indicate that SRS and CBET will also be reduced. On the other hand, the laser energy saved from a reduced CBET effect may become available to contribute to TPD and SRS growth.

Simulations of single-mode perturbations have demonstrated that mid-Z-ablator–ignition designs and plastic designs have similar hydrodynamic stability properties. Multimode simulations indicate that the three targets are robust to both the inner-ice-surface and outer-surface roughnesses well above the NIF specifications. The overall stability of these targets to laser-imprint perturbations exhibits enough margin to achieve ignition and high gains for a uniform drive. Using a mid-Z ablator does not appear to mitigate the RT growth of perturbations seeded by either fabrication defects or laser-drive nonuniformities for ignition-scale target designs. For more-realistic laser irradiation, a polar-direct-drive configuration has been developed for each design within the NIF laser specifications. The relative energy among the beams, the pulse shapes, the beam pointing, and the beam spot shapes were varied to find an optimal configuration for the target drive uniformity, resulting in ignition and high target gains. Therefore, mid-Z ablator targets represent a viable option for direct-drive–ignition designs since they present better overall performances than plastic ablators by decreasing the detrimental effects of LPI on the implosion without a significant degradation of hydrodynamic stability properties.

ACKNOWLEDGMENT

This work was supported by the U.S. Department of Energy National Nuclear Security Administration under Award Numbers DE-NA0001944 and DE-FC02-04ER54789, the University of Rochester, and the New York State Energy Research and Development Authority. The support of DOE does not constitute an endorsement by DOE of the views expressed in this article.

REFERENCES

1. J. D. Lindl, *Inertial Confinement Fusion: The Quest for Ignition and Energy Gain Using Indirect Drive* (Springer-Verlag, New York, 1998).
2. S. Atzeni and J. Meyer-ter-Vehn, *The Physics of Inertial Fusion: Beam Plasma Interaction, Hydrodynamics, Hot Dense Matter*, International Series of Monographs on Physics (Clarendon Press, Oxford, 2004).
3. G. H. Miller, E. I. Moses, and C. R. Wuest, Opt. Eng. **43**, 2841 (2004).
4. M. V. Goldman, Ann. Phys. **38**, 117 (1966).
5. T. R. Boehly, D. L. Brown, R. S. Craxton, R. L. Keck, J. P. Knauer, J. H. Kelly, T. J. Kessler, S. A. Kumpan, S. J. Loucks, S. A. Letzring, F. J. Marshall, R. L. McCrory, S. F. B. Morse, W. Seka, J. M. Soures, and C. P. Verdon, Opt. Commun. **133**, 495 (1997).
6. R. L. McCrory, D. D. Meyerhofer, R. Betti, R. S. Craxton, J. A. Delettrez, D. H. Edgell, V. Yu. Glebov, V. N. Goncharov, D. R. Harding, D. W. Jacobs-Perkins, J. P. Knauer, F. J. Marshall, P. W. McKenty, P. B. Radha, S. P. Regan, T. C. Sangster, W. Seka, R. W. Short, S. Skupsky, V. A. Smalyuk, J. M. Soures, C. Stoeckl, B. Yaakobi, D. Shvarts, J. A. Frenje, C. K. Li, R. D. Petrasso, and F. H. Séguin, Phys. Plasmas **15**, 055503 (2008).
7. V. A. Smalyuk, D. Shvarts, R. Betti, J. A. Delettrez, D. H. Edgell, V. Yu. Glebov, V. N. Goncharov, R. L. McCrory, D. D. Meyerhofer, P. B. Radha, S. P. Regan, T. C. Sangster, W. Seka, S. Skupsky, C. Stoeckl, B. Yaakobi, J. A. Frenje, C. K. Li, R. D. Petrasso, and F. H. Séguin, Phys. Rev. Lett. **100**, 185005 (2008).
8. T. C. Sangster, V. N. Goncharov, P. B. Radha, V. A. Smalyuk, R. Betti, R. S. Craxton, J. A. Delettrez, D. H. Edgell, V. Yu. Glebov, D. R. Harding, D. Jacobs-Perkins, J. P. Knauer, F. J. Marshall, R. L. McCrory, P. W. McKenty, D. D. Meyerhofer, S. P. Regan, W. Seka, R. W. Short, S. Skupsky, J. M. Soures, C. Stoeckl, B. Yaakobi, D. Shvarts, J. A. Frenje, C. K. Li, R. D. Petrasso, and F. H. Séguin, Phys. Rev. Lett. **100**, 185006 (2008).
9. Lord Rayleigh, Proc. London Math Soc. **XIV**, 170 (1883).
10. G. Taylor, Proc. R. Soc. London Ser. A **201**, 192 (1950).
11. H. Takabe *et al.*, Phys. Fluids **28**, 3676 (1985).
12. R. Betti, V. N. Goncharov, R. L. McCrory, and C. P. Verdon, Phys. Plasmas **5**, 1446 (1998).
13. S. Fujioka *et al.*, Phys. Plasmas **11**, 2814 (2004).
14. J. Sanz, R. Betti, V. A. Smalyuk, M. Olazabal-Loume, V. Drean, V. Tikhonchuk, X. Ribeyre, and J. Feugeas, Phys. Plasmas **16**, 082704 (2009).
15. A. Simon, R. W. Short, E. A. Williams, and T. Dewandre, Phys. Fluids **26**, 3107 (1983).
16. V. A. Smalyuk, R. Betti, J. A. Delettrez, V. Yu. Glebov, D. D. Meyerhofer, P. B. Radha, S. P. Regan, T. C. Sangster, J. Sanz, W. Seka, C. Stoeckl, B. Yaakobi, J. A. Frenje, C. K. Li, R. D. Petrasso, and F. H. Séguin, Phys. Rev. Lett. **104**, 165002 (2010).
17. S. X. Hu, D. T. Michel, D. H. Edgell, D. H. Froula, R. K. Follett, V. N. Goncharov, J. F. Myatt, S. Skupsky, and B. Yaakobi, Phys. Plasmas **20**, 032704 (2013).
18. D. H. Froula, D. T. Michel, I. V. Igumenshchev, S. X. Hu, B. Yaakobi, J. F. Myatt, D. H. Edgell, R. Follett, V. Yu. Glebov, V. N. Goncharov, T. J. Kessler, A. V. Maximov, P. B. Radha, T. C. Sangster, W. Seka, R. W. Short, A. A. Solodov, C. Sorce, and C. Stoeckl, Plasma Phys. Control. Fusion **54**, 124016 (2012).
19. P. B. Radha, J. P. Knauer, T. C. Sangster, V. N. Goncharov, I. V. Igumenshchev, R. Betti, R. Epstein, D. D. Meyerhofer, and S. Skupsky, Bull. Am. Phys. Soc. **52**, 143 (2007).
20. S. X. Hu, G. Fiksel, V. N. Goncharov, S. Skupsky, D. D. Meyerhofer, and V. A. Smalyuk, Phys. Rev. Lett. **108**, 195003 (2012).
21. G. Fiksel, S. X. Hu, V. N. Goncharov, D. D. Meyerhofer, T. C. Sangster, V. A. Smalyuk, B. Yaakobi, M. J. Bonino, and R. Jungquist, Phys. Plasmas **19**, 062704 (2012).
22. J. P. Knauer, P. B. Radha, V. N. Goncharov, I. V. Igumenshchev, R. Betti, R. Epstein, F. J. Marshall, S. P. Regan, V. A. Smalyuk, D. D. Meyerhofer, and S. Skupsky, Bull. Am. Phys. Soc. **52**, 233 (2007).
23. C. Stoeckl, J. A. Delettrez, J. H. Kelly, T. J. Kessler, B. E. Kruschwitz, S. J. Loucks, R. L. McCrory, D. D. Meyerhofer, D. N. Maywar, S. F. B. Morse, J. Myatt, A. L. Rigatti, L. J. Waxer, J. D. Zuegel, and R. B. Stephens, Fusion Sci. Technol. **49**, 367 (2006).
24. T. J. B. Collins, J. A. Marozas, K. S. Anderson, R. Betti, R. S. Craxton, J. A. Delettrez, V. N. Goncharov, D. R. Harding, F. J. Marshall, R. L. McCrory, D. D. Meyerhofer, P. W. McKenty, P. B. Radha, A. Shvydky, S. Skupsky, and J. D. Zuegel, Phys. Plasmas **19**, 056308 (2012).
25. J. Delettrez, R. Epstein, M. C. Richardson, P. A. Jaanimagi, and B. L. Henke, Phys. Rev. A **36**, 3926 (1987).
26. R. E. Kidder, Nucl. Fusion **14**, 53 (1974).
27. B. Strömgren, Z. Astrophys. **4**, 118 (1932).
28. B. F. Rozsnyai, Phys. Rev. A **5**, 1137 (1972).
29. R. Epstein, T. J. B. Collins, J. A. Delettrez, S. Skupsky, and R. P. J. Town, Bull. Am. Phys. Soc. **43**, 1666 (1998).
30. B. I. Bennett *et al.*, Los Alamos National Laboratory, Los Alamos, NM, Report LA-7130 (1978).
31. W. F. Huebner *et al.*, Los Alamos National Laboratory, Los Alamos, NM, Report LA-6760-M (1977).
32. L. Spitzer, Jr. and R. Härm, Phys. Rev. **89**, 977 (1953).
33. Prism Computational Sciences, Inc., Madison, WI 53711.
34. *LLE Review Quarterly Report* **133**, 1, Laboratory for Laser Energetics, University of Rochester, Rochester, NY, LLE Document No. DOE/NA/28302-1093 (2012).
35. P. Chang, K. Anderson, and R. Betti, Bull. Am. Phys. Soc. **54**, 260 (2009).

36. B. Yaakobi, A. A. Solodov, J. F. Myatt, J. A. Delettrez, C. Stoeckl, and D. H. Froula, Phys. Plasmas **20**, 092706 (2013).

37. D. H. Froula, B. Yaakobi, S. X. Hu, P.-Y. Chang, R. S. Craxton, D. H. Edgell, R. Follett, D. T. Michel, J. F. Myatt, W. Seka, R. W. Short, A. Solodov, and C. Stoeckl, Phys. Rev. Lett. **108**, 165003 (2012).

38. D. T. Michel, A. V. Maximov, R. W. Short, S. X. Hu, J. F. Myatt, W. Seka, A. A. Solodov, B. Yaakobi, and D. H. Froula, Phys. Rev. Lett. **109**, 155007 (2012).

39. B. Yaakobi, P.-Y. Chang, A. A. Solodov, C. Stoeckl, D. H. Edgell, R. S. Craxton, S. X. Hu, J. F. Myatt, F. J. Marshall, W. Seka, and D. H. Froula, Phys. Plasmas **19**, 012704 (2012).

40. J. F. Myatt, J. Zhang, J. A. Delettrez, A. V. Maximov, R. W. Short, W. Seka, D. H. Edgell, D. F. DuBois, D. A. Russell, and H. X. Vu, Phys. Plasmas **19**, 022707 (2012).

41. D. F. DuBois, D. A. Russell, and H. A. Rose, Phys. Rev. Lett. **74**, 3983 (1995).

42. D. A. Russell and D. F. DuBois, Phys. Rev. Lett. **86**, 428 (2001).

43. J. F. Myatt, H. X. Vu, D. F. DuBois, D. A. Russell, J. Zhang, R. W. Short, and A. V. Maximov, Phys. Plasmas **20**, 052705 (2013).

44. W. Theobald, R. Nora, M. Lafon, A. Casner, X. Ribeyre, K. S. Anderson, R. Betti, J. A. Delettrez, J. A. Frenje, V. Yu. Glebov, O. V. Gotchev, M. Hohenberger, S. X. Hu, F. J. Marshall, D. D. Meyerhofer, T. C. Sangster, G. Schurtz, W. Seka, V. A. Smalyuk, C. Stoeckl, and B. Yaakobi, Phys. Plasmas **19**, 102706 (2012).

45. H. A. Baldis, E. M. Campbell, and W. L. Kruer, in *Handbook of Plasma Physics*, edited by M. N. Rosenbluth and R. Z. Sagdeev, Vol. 3: Physics of Laser Plasma, edited by A. Rubenchik and S. Witkowski (North-Holland, Amsterdam, 1991), Chap. 9, p. 377.

46. I. V. Igumenshchev, D. H. Edgell, V. N. Goncharov, J. A. Delettrez, A. V. Maximov, J. F. Myatt, W. Seka, A. Shvydky, S. Skupsky, and C. Stoeckl, Phys. Plasmas **17**, 122708 (2010).

47. I. V. Igumenshchev, D. H. Froula, D. H. Edgell, V. N. Goncharov, T. J. Kessler, F. J. Marshall, R. L. McCrory, P. W. McKenty, D. D. Meyerhofer, D. T. Michel, T. C. Sangster, W. Seka, and S. Skupsky, Phys. Rev. Lett. **110**, 145001 (2013).

48. C. Yañez *et al.*, Phys. Plasmas **18**, 052701 (2011).

49. V. Drean *et al.*, Phys. Plasmas **17**, 122701 (2010).

50. S. Fujioka *et al.*, Phys. Rev. Lett. **92**, 195001 (2004).

51. P. B. Radha, V. N. Goncharov, T. J. B. Collins, J. A. Delettrez, Y. Elbaz, V. Yu. Glebov, R. L. Keck, D. E. Keller, J. P. Knauer, J. A. Marozas, F. J. Marshall, P. W. McKenty, D. D. Meyerhofer, S. P. Regan, T. C. Sangster, D. Shvarts, S. Skupsky, Y. Srebro, R. P. J. Town, and C. Stoeckl, Phys. Plasmas **12**, 032702 (2005).

52. J. D. Hager, T. J. B. Collins, V. A. Smalyuk, J. P. Knauer, D. D. Meyerhofer, and T. C. Sangster, Phys. Plasmas **20**, 072707 (2013).

53. S. Skupsky, R. W. Short, T. Kessler, R. S. Craxton, S. Letzring, and J. M. Soures, J. Appl. Phys. **66**, 3456 (1989).

54. S. Skupsky, J. A. Marozas, R. S. Craxton, R. Betti, T. J. B. Collins, J. A. Delettrez, V. N. Goncharov, P. W. McKenty, P. B. Radha, T. R. Boehly, J. P. Knauer, F. J. Marshall, D. R. Harding, J. D. Kilkenny, D. D. Meyerhofer, T. C. Sangster, and R. L. McCrory, Phys. Plasmas **11**, 2763 (2004).

55. J. A. Marozas, F. J. Marshall, R. S. Craxton, I. V. Igumenshchev, S. Skupsky, M. J. Bonino, T. J. B. Collins, R. Epstein, V. Yu. Glebov, D. Jacobs-Perkins, J. P. Knauer, R. L. McCrory, P. W. McKenty, D. D. Meyerhofer, S. G. Noyes, P. B. Radha, T. C. Sangster, W. Seka, and V. A. Smalyuk, Phys. Plasmas **13**, 056311 (2006).

56. A. M. Cok, R. S. Craxton, and P. W. McKenty, Phys. Plasmas **15**, 082705 (2008).

57. N. S. Krasheninnikova, S. M. Finnegan, and M. J. Schmitt, Phys. Plasmas **19**, 012702 (2012).

58. P. B. Radha, J. A. Marozas, F. J. Marshall, A. Shvydky, T. J. B. Collins, V. N. Goncharov, R. L. McCrory, P. W. McKenty, D. D. Meyerhofer, T. C. Sangster, and S. Skupsky, Phys. Plasmas **19**, 082704 (2012).

59. K. S. Anderson, R. Betti, P. W. McKenty, T. J. B. Collins, M. Hohenberger, W. Theobald, R. S. Craxton, J. A. Delettrez, M. Lafon, J. A. Marozas, R. Nora, S. Skupsky, and A. Shvydky, Phys. Plasmas **20**, 056312 (2013).

60. N. S. Krasheninnikova *et al.*, Phys. Plasmas **21**, 042703 (2014).

61. R. S. Craxton, F. J. Marshall, M. J. Bonino, R. Epstein, P. W. McKenty, S. Skupsky, J. A. Delettrez, I. V. Igumenshchev, D. W. Jacobs-Perkins, J. P. Knauer, J. A. Marozas, P. B. Radha, and W. Seka, Phys. Plasmas **12**, 056304 (2005).

62. R. S. Craxton and D. W. Jacobs-Perkins, Phys. Rev. Lett. **94**, 095002 (2005).

63. P. B. Radha, F. J. Marshall, J. A. Marozas, A. Shvydky, I. Gabalski, T. R. Boehly, T. J. B. Collins, R. S. Craxton, D. H. Edgell, R. Epstein, J. A. Frenje, D. H. Froula, V. N. Goncharov, M. Hohenberger, R. L. McCrory, P. W. McKenty, D. D. Meyerhofer, R. D. Petrasso, T. C. Sangster, and S. Skupsky, Phys. Plasmas **20**, 056306 (2013).

64. M. J. Schmitt, P. A. Bradley, J. A. Cobble, J. R. Fincke, P. Hakel, S. C. Hsu, N. S. Krasheninnikova, G. A. Kyrala, G. R. Magelssen, D. S. Montgomery, T. J. Murphy, K. A. Obrey, R. C. Shah, I. L. Tregillis, J. A. Baumgaertel, F. J. Wysocki, S. H. Batha, R. S. Craxton, P. W. McKenty, P. Fitzsimmons, A. Nikroo, and R. Wallace, Phys. Plasmas **20**, 056310 (2013).

65. G. P. Schurtz, Ph. D. Nicolaï, and M. Busquet, Phys. Plasmas **7**, 4238 (2000).

66. J. A. Delettrez, T. J. B. Collins, P. B. Radha, D. T. Michel, D. Cao, and G. Moses, Bull. Am. Phys. Soc. **58**, 323 (2013).